Investigation of thermal large-eddy simulation approaches in a highly turbulent channel flow submitted to strong asymmetric heating

M. David, Adrien Toutant, Françoise Bataille

Investigation of Thermal Large-Eddy Simulation approaches in a highly turbulent channel flow submitted to strong asymmetric heating

M.David,[1, a)] A.Toutant,[1, b)] and F. Bataille[1, c)]
PROMES-CNRS laboratory (UPR 8521), Université de Perpignan via Domitia, Technosud-Rambla de la thermodynamique, 66100 Perpignan, France

(Dated: 14 February 2021)

This study deals with Thermal Large-Eddy Simulation (T-LES) of anisothermal turbulent channel flow in the working conditions of solar receivers used in concentrated solar power towers. The flow is characterized by high-temperature levels and strong heat fluxes. The hot and cold friction Reynolds numbers of the simulations are respectively 630 and 970. The Navier-Stokes equations are solved under the low Mach number approximation and the thermal dilatation is taken into account. The momentum convection and the density-velocity correlation subgrid terms are modeled. Functional, structural, and mixed subgrid-scale models are investigated. A tensorial version of the classical Anisotropic Minimum-Dissipation (AMD) model is studied and produces good results. A Quick scheme and a second-order centered scheme are tested for the discretization of the mass convection term. Firstly, a global assessment of 22 large-eddy simulations is proposed then 6 are selected for a careful analysis including profiles of mean quantities and fluctuation values as well as a comparison of instantaneous fields. Probability density functions of wall heat fluxes are plotted. The results point out that thermal large-eddy simulations performed with the Quick scheme tend to underestimate the wall heat flux whereas the second-order centered scheme significantly improves its estimation. Thermal large-eddy simulations tend to overestimate the peaks of velocity correlations. When regarding the dimensionless profiles of fluctuations, the tensorial AMD model provides better results than the other assessed models. For the heat flux estimation, the best agreement is found with the AMD model combined with the second-order centered scheme.

I. INTRODUCTION

This study falls within the research on the solar receivers of concentrated solar power towers. The solar receiver is crossed by an asymmetrically heated and highly turbulent airflow. Turbulent flows submitted to asymmetric heating are a challenging field of research. They are ubiquitous in many application fields such as heat exchangers, nuclear reactors, electronic devices, and solar receivers. Turbulence is described by the equations of Navier-Stokes. The complexity of these equations renders the Direct Numerical Simulations (DNS) of turbulence inapplicable to most of systems because of the required computational cost. Thermal large-eddy simulation (T-LES) is a family of methods aiming to obtain a low-cost three-dimensional unsteady simulation of an anisothermal turbulent flow. Large scales are explicitly resolved, while small scales, more computationally expensive to resolve, are accounted for by their modeled effect on larger scales. The separation between resolved and modeled scales is generally performed using a low-pass filter. Subgrid models are necessary to close the governing equations. In this paper, we assess various turbulence models of T-LES in an asymmetrically heated turbulent channel flow under the low Mach number approximation. Fully developed channel flow is a popular test case for subgrid models of LES[1–16]. This geometry appears as a good test case for turbulence model because of its near-wall behavior presenting small coherent scales in the viscous sublayer. The working conditions studied are close to the ones encountered in existing solar receivers. They are characterized by highly turbulent airflow, asymmetrical heating, high-temperature levels, and strong heat fluxes.

In 1996, Wang and Pletcher[17] were the first authors to perform LES of channel flows with high-heat transfer rates at low-Mach and low-Reynolds numbers. They use the incompressible dynamic subgrid-scale (SGS) model of Germano *et al.*[18] extended to compressible case by Moin *et al.*[19]. Two wall temperature ratios were tested: 1.02 and 3.0. They show that the temperature-velocity correlations are very dependent on the heat transfer rate. The velocity fluctuations are enhanced with heating. However, the temperature fluctuations are bigger at the cold wall when scaled by the local mean quantities. Nicoud[20] tests three finite-difference schemes to solve the Navier-Stokes equations under the low-Mach number approximation. The friction Reynolds number is 180. The assessed algorithms are algorithms with low numerical dissipation. They exhibit fourth-order spatial and second-order temporal accuracy. A variable coefficient Poisson equation is used to solve the pressure equation. The author carries out simulations with temperature ratios of 1.01, 2, 4, 6, 8, and 10. The three tested algorithms are stable for the three first temperature ratios. Daileys *et al.*[9] perform LES at constant wall heat flux using a compressible solver at a bulk Reynolds number of 11000. The mass flow rate is imposed. The wall-to-bulk temperature ratios are 1.05 and 1.48 for the heated case and 0.56 for the cooled case. As Wang and Pletcher[17], the authors use the incompressible dynamic SGS model of Germano *et al.*[18] extended to compressible case by Moin *et al.*[19]. They point out that heating and cooling influence the mean velocity and temperature profiles. The bigger the wall-to-bulk temperature ratio is, the smaller the average turbulent kinetic is. The friction velocity is 26 percent higher in the high heating case and 27 percent lower in the high cooling case as compared to

[a)]Electronic mail: martin.david@promes.cnrs.fr
[b)]Electronic mail: Author to whom correspondence should be addressed: adrien.toutant@promes.cnrs.fr
[c)]Electronic mail: francoise.bataille@promes.cnrs.fr

the low heating results. Moreover, the peaks of resolved turbulent stress are slightly larger for the high cooling case compared to the low heating results. Lessani and Papalexandris[21] focus their attention on channel flows at high wall temperature ratios. They do not consider compressibility effects meaning that the density variations are only influenced by temperature variations. The Navier-Stokes equations are solved under the low-Mach number approximation. In their working condition, the friction Reynolds number is 180. As Daileys *et al.*[9] and Wang and Pletcher[17], they notice that the mean velocity profile on the cold side deviates from the isothermal logarithmic law of the wall. However, the hot side is near the incompressible isothermal law of the wall. The turbulent kinetic energy in the near-wall region is higher on the cold side than on the hot side meaning that heating tends to laminarize the flow. The temperature fluctuations are more intense near the cold wall. The biggest peak of temperature fluctuations is observed on the hot side but far from the wall. Bellec *et al.*[22] investigate the thermal boundary layer spatial developments in a turbulent channel flow submitted to asymmetric heating using LES. Wall temperatures are 590 K and 380 K. The friction Reynolds number is 395. The Wall-Adapting Local Eddy-viscosity (WALE) model proposed by Nicoud and Ducros[23] is used. They highlight that the coupling between temperature and velocity fields modifies both the mean and the fluctuations profiles. The fluid heating tends to reduce the peak of classically scaled fluctuations of the three components of velocity compared to an isothermal case. Serra *et al.*[7] study an asymmetrically heated turbulent channel flow with imposed wall temperatures. The temperature ratios are 1.01, 1.07, and 2. Simulations are performed for two friction Reynolds numbers: 180 and 395. Navier-Stokes equations are solved under the low-Mach number approximation. As in the study of Bellec *et al.*[22], the WALE model of Nicoud and Ducros[23] is used. The authors investigate the impact of thermal gradients. For low-temperature ratios (1.01 and 1.07), the variations of the viscosity and the conductivity can be fixed at constant values. The authors mention that the constant subgrid-scale Prandtl number and the dynamic calculation of the subgrid-scale Prandtl number produce similar results. As in Refs.[9,17,21], the temperature ratio modify the mean profiles, the fluctuations and the correlations. Yahya *et al.*[24] investigate turbulent forced convective flow in an anisothermal channel at low-Mach thanks to the WALE subgrid model[23]. Results for four friction Reynolds numbers are presented: 150, 180, 245, and 460. The wall temperature ratio varies between 1.01 and 5. They point out that turbulence is enhanced at the cold side. The turbulent kinetic energy is lower at the hot wall than at the cold wall. They also notice that the turbulent structures are very short and densely populated in the vicinity of the cold wall. Near the hot wall, turbulence produces large elongated vortices and long streaky structures. For high-temperature ratio and low friction Reynolds number, they observe relaminarization of the fluid at the hot side. Serra *et al.*[25] propose a summary of works on non-isothermal turbulent flows with asymmetric wall temperatures.

A posteriori tests are widely studied in the literature. They are considered to be the ultimate tests of model performance since they consider all the simulation factors (combining effects of numerical discretization, time integration, and averaging)[26]. For that reason, we carry out *a posteriori* tests of the subgrid models to assess their efficiency. Few *a posteriori* tests dealing with isotropic turbulence are described below. Kosović *et al.*[27] perform LES of decaying isotropic turbulence on a periodic cubic domain. They study two phenomenological subgrid-scale models using *a posteriori* tests of compressible turbulent flow. Hickel *et al.*[28] proposed an *a posteriori* analysis of the spectral numerical dissipation in simulations of freely decaying homogeneous isotropic turbulence. Vashishtha *et al.*[29] used renormalized viscosity to perform LES of decaying homogeneous and isotropic turbulence in a cubical domain. They compare LES and DNS results and show that the LES is able to capture the evolution of total energy and total dissipation rate as well as the energy spectrum and flux. Isothermal wall-bounded turbulent flows are also widely encountered in the literature. Dupuy *et al.*[5] perform *a posteriori* tests of subgrid-scale models in an isothermal turbulent channel. They assess five functional eddy-viscosity models (Wall-Adapting Local Eddy-viscosity, Sigma, Anisotropic Minimum-Dissipation, Kobayashi, and anisotropic Smagorinsky) and two structural models (gradient and scale-similarity). The gradient model is found to be not sufficiently impactful to significantly alter the flow. It must be filtered and amplified. The turbulence anisotropy is poorly represented by functional models. They also test dynamic versions of models but they do not notably improve the prediction of models. The Anisotropic Minimum-Dissipation (AMD) tensorial eddy-viscosity model provides good results on the wall shear stress and the turbulence anisotropy. Horiuti[30] investigates the Bardina model[31] in turbulent isothermal channel flow. Thanks to *a posteriori* tests, he shows that this model has a strong negative correlation with the Leonard term for the SGS cross-stress term. The Bardina model plays a role as a backscattering of subgrid-scale energy in the buffer layer, which considerably improves the accuracy of LES. Stolz *et al.*[32] employs both *a priori* and *a posteriori* analysis to test an approximate deconvolution model for the large-eddy simulation of incompressible flows. Some studies also involve this type of test to evaluate particular LES methods and to quantify the LES sensitivity to simulation parameters. For instance, Vreman *et al.*[33] compare LES of the temporal mixing layer with *a posteriori* tests using the dynamic mixed model in combination with five different numerical schemes. They point out that the numerical method has a strong influence on the results. Rezaeiravesh *et al.*[34] also mention the major role of numerical error. Indeed, in the working conditions studied by the authors, the errors induced by the WALE subgrid-scale model are dominated by the numerical error. Geurts and van der Bos[35] investigate explicit filtering. They show that the numerical high-pass effects are dependent on the subfilter resolution, defined as the ratio of filter width and grid spacing. The more the filter width is close to the grid spacing, the more the numerically effects are salient. For a ratio between 1 and 2, the induced numerically effects are comparable to, or even larger than the turbulent stresses. Kremer *et al.*[36] assess the resolution requirement and Reynolds number effects of tur-

bulent channel flow using relaxation filtering. *A posteriori* tests indicate that LES using relaxation filtering approach is efficient to simulate fully turbulent wall-bounded flows provided that grid resolution is sufficient and that largest scales are not overly affected by numerical dissipation. Another example is the work of Keating *et al.*[37] which combines *a priori* and *a posteriori* tests to compare three inflow conditions of turbulent wall-bounded flow. The authors investigate a synthetic turbulence generation method, a recycling method, and a forcing method including a control loop. This last method is found to be effective by generating turbulence with the correct Reynolds stresses and correlations within less than ten channel half heights.

It seems that very few studies are assessing LES subgrid-scale models with *a posteriori* tests of anisothermal channel flow. Dupuy *et al.*[4] perform T-LES in strongly anisothermal turbulent channel flows. The ratio of wall temperatures is 2. They solve the Navier-Stokes equations under the low-Mach number approximation in two formulations: the velocity formulation and the Favre formulation. Both the momentum convection subgrid term and the density-velocity correlation subgrid term are modeled. They study functional eddy-viscosity or eddy-diffusivity models, structural models, tensorial models, and dynamic versions of these models at friction Reynolds number of 180 and 395. The best results are obtained with the Favre formulation. Among the tested models, the AMD and the scale-similarity approaches are the most satisfying. To the author's knowledge, there is no *a posteriori* test of LES subgrid models in a highly turbulent channel flow submitted to asymmetric heating. This paper aims to fulfill this gap in the literature by assessing T-LES models in the discussed working conditions.

The outline of this paper is as follows: in Sec.II, the resolved equations are expressed. The investigated subgrid-scale models are described in Sec.III. The channel flow configuration and the numerical method are presented in Sec.IV. The results of the models are summarized and discussed in Sec.V. Then, six T-LES approaches are selected for an accurate study.

II. FILTERED LOW-MACH NUMBER EQUATIONS

In this section, we present the formalism of the resolved equations. Following the recommendations of Dupuy *et al.*[4] we use the Favre formulation to filter the equations. It involves Favre-filtered variables, based on the density-weighted Favre filter ($\widetilde{\cdot}$). The variables are defined for any field ψ as $\widetilde{\psi} = \overline{\rho\psi}/\overline{\rho}$, where ($\overline{\cdot}$) is the unweighted classical filter. The two most significant subgrid terms mentioned by Dupuy *et al.*[6] are considered: a subgrid term related to the nonlinearity of momentum convection and another modeling the correlation of density and velocity. The low-Mach number Navier-Stokes equations admit large variations in gas density while remain acoustically incompressible[38]. This approximation, well adapted to the studied conditions, introduces two pressures: the mechanical pressure and the thermodynamical pressure which is homogeneous. The low Mach number hypothesis permits to reduce the computational time to reach convergence by increasing the fractionnal timestep when compared to as the resolution of the compressible Navier-Stokes equations. The Stokes' hypothesis is assumed. See Papalexandris for further details on the applicability of the Stokes' hypothesis to low Mach number flows[39]. The solved equations are presented below.

- Mass conservation equation

$$\frac{\partial \overline{\rho}}{\partial t} + \frac{\partial \overline{\rho}\widetilde{U}_j}{\partial x_j} = 0, \tag{1}$$

- Momentum conservation equation

$$\frac{\partial \overline{\rho}\widetilde{U}_i}{\partial t} = -\frac{(\partial \overline{\rho}\widetilde{U}_j\widetilde{U}_i + \rho G_{U_jU_i})}{\partial x_j} - \frac{\partial P}{\partial x_i} + \frac{\partial \Sigma_{ij}(\widetilde{\boldsymbol{U}},\widetilde{T})}{\partial x_j}, \tag{2}$$

- Energy conservation equation

$$\frac{\partial}{\partial x_j}(\widetilde{U}_j + \overline{\rho}G_{U_j/\rho}) = -\frac{1}{\gamma P_0}\left[(\gamma-1)\frac{\partial Q_j(\widetilde{T})}{\partial x_j} + \frac{\mathrm{d}P_0}{\mathrm{d}t}\right], \tag{3}$$

- Ideal gas law

$$\widetilde{T} = \frac{P_0}{\overline{\rho} r} \tag{4}$$

where ρ is the density, T is the temperature, γ is the heat capacity ratio, $r = 330\ \mathrm{J.kg^{-1}.K^{-1}}$ is the ideal gas specific constant, t is the time, P is the mechanical pressure, P_0 the thermodynamical pressure, U_i is the ith component of velocity, $\mathrm{d}/\mathrm{d}t$ is the time derivative (total derivative since P_0 is homogeneous), and x_i is the Cartesian coordinate in the ith direction. The subgrid term relative to momentum convection is $G_{U_jU_i} = \widetilde{U_jU_i} - \widetilde{U}_j\widetilde{U}_i$ and the subgrid term relative to the density-velocity correlation is expressed as $G_{U_j/\rho} = \widetilde{U_j/\rho} - \widetilde{U}_j/\overline{\rho}$. The Einstein summation convention is used. The functions $\Sigma_{ij}(\widetilde{\boldsymbol{U}},\widetilde{T})$ and $Q_j(\widetilde{T})$ are used to compute the shear-stress tensor and conductive heat flux associated with a given velocity and temperature. The particular form of the energy conservation equation, involving the velocity divergence, is obtained (1) by applying the ideal gas law to the energy equation written in terms of transport of temperature; (2) by using the fact that the thermodynamical pressure is homogeneous. This formulation is also used by Nicoud[20] and Dupuy *et al.*[4]. The thermodynamical pressure is computed by integrating Eq. 3 over the volume of the computational domain:

$$\frac{\mathrm{d}P_0}{\mathrm{d}t} = -\frac{\gamma-1}{V}\int Q_j(\widetilde{T})\mathrm{d}S_j \tag{5}$$

where V is the volume of the computational domain and S_j are the boundaries of the computational domain.

Newtonian fluid and Fourier's law are assumed, leading to the following expressions:

$$\Sigma_{ij}(\widetilde{\boldsymbol{U}},\widetilde{T}) = \mu(\widetilde{T})\left(\frac{\partial \widetilde{U}_i}{\partial x_j} + \frac{\partial \widetilde{U}_j}{\partial x_i}\right) - \frac{2}{3}\mu(\widetilde{T})\frac{\partial \widetilde{U}_k}{\partial x_k}\delta_{ij}, \tag{6}$$

$$Q_j(\widetilde{T}) = -\lambda(\widetilde{T})\frac{\partial \widetilde{T}}{\partial x_j}, \tag{7}$$

with $\mu(\widetilde{T})$ as the dynamic viscosity, $\lambda(\widetilde{T})$ as the thermal conductivity, and δ_{ij} as the Kronecker symbol.

The fluid used is air. The viscosity is computed using the Sutherland's law[40].

$$\mu(\widetilde{T}) = \mu_0 \frac{\widetilde{T}}{T_0}^{3/2} \frac{T_0+S}{\widetilde{T}+S}, \tag{8}$$

where $\mu_0 = 1.716\times10^{-5}$ $Pa.s$, $S = 110.4$ K, and $T_0 = 273.15$ K. The Prandtl number is supposed to be constant, $Pr = 0.87$ and the heat capacity at constant pressure $C_p = 1155$ J.kg^{-1}.K^{-1}. The conductivity is deduced from the Prandtl number, the heat capacity at constant pressure, and the viscosity.

$$\lambda(\widetilde{T}) = \frac{C_p}{Pr}\mu(\widetilde{T}). \tag{9}$$

III. SUBGRID-SCALE MODELS

The following formalism is introduced to express the models for momentum convection subgrid term and density-velocity correlation subgrid term.

$$G_{U_jU_i} \approx \tau_{ij}^{mod}(\widetilde{U},\overline{\Delta}) \tag{10}$$

$$G_{U_j/\rho} \approx \pi_j^{mod}(\widetilde{\mathbf{U}},1/\overline{\rho},\overline{\Delta}) \tag{11}$$

The subgrid-scale tensors, τ_{ij} and π_{ij}, are computed thanks to variables resolved in T-LES. The function used to compute the subgrid-scale tensor depends on the model used. In this study, zero algebraic models without wall function or wall model are investigated. Functional, structural, and mixed models are assessed. They are listed in the following subsections. In the following of this article, the filter length scale is computed using $\overline{\Delta} = \left(\overline{\Delta}_x\overline{\Delta}_y\overline{\Delta}_z\right)^{1/3}$. The filter length scale and the mesh size are equal.

A. Functional models

Functional modeling consists in reproducing the action of the subgrid terms by introducing a term that have a similar effect. This term does not have necessarily the same structure as the subgrid tensor. In functional modeling, the action of the subgrid scales on the resolved scales is mainly an energetic action. This approach does not consider the backward energy cascade and is often over-dissipative. The subgrid-scale tensor relative to momentum convection is computed by analogy with molecular diffusion:

$$\tau_{ij}^{mod}(\widetilde{U},\overline{\Delta}) = -2\nu_t^{mod}(\mathbf{g},\mathbf{d},\overline{\Delta})S_{ij}, \tag{12}$$

where $S_{ij} = 0.5(g_{ij}+g_{ji})$ is the rate of the deformation tensor, $\mathbf{g}$ is the velocity gradient: $g_{ij} = \partial\widetilde{U}_i/\partial x_j$, and ν_t^{mod} is the turbulent viscosity whose expression depends on the model used. The eddy-diffusivity models are used for the density-velocity subgrid term. They involves the subgrid-scale Prandtl number, Pr_t:

$$\pi_j^{mod}(\widetilde{U},\phi,\overline{\Delta}) = -\frac{\nu_t^{mod}(\mathbf{g},\mathbf{d},\overline{\Delta})}{Pr_t}d_j \tag{13}$$

with $\boldsymbol{d_j} = \partial\phi/\partial x_j$ the scalar gradient. Pr_t is the turbulent Prandtl number and is equal to 0.9.

The following eddy-viscosity models are studied in this paper.

- WALE model[23]

$$\nu_t^{WALE}\left(\mathbf{g},\mathbf{d},\overline{\Delta}\right) = \left(C^{WALE}\overline{\Delta}\right)^2 \frac{\left(S_{ij}^dS_{ij}^d\right)^{3/2}}{\left(S_{mn}S_{mn}\right)^{5/2}+\left(S_{mn}^dS_{mn}^d\right)^{5/4}} \tag{14}$$

- AMD[12]

$$\nu_t^{AMD}\left(\mathbf{g},\mathbf{d},\overline{\Delta}\right) = C^{AMD}\frac{max(0,-G_{ij}S_{ij})}{g_{mn}g_{mn}} \tag{15}$$

- Scalar AMD model[41]

$$\nu_t^{AMD}\left(\mathbf{g},\mathbf{d},\overline{\Delta}\right) = C^{AMDs}\frac{max(0,-D_jd_j)}{d_md_m} \tag{16}$$

- Sigma[16]

$$\nu_t^{Sigma}\left(\mathbf{g},\mathbf{d},\overline{\Delta}\right) = \left(C^{Sigma}\overline{\Delta}\right)^2 \frac{\sigma_3(\sigma_1-\sigma_2)(\sigma_2-\sigma_3)}{\sigma_1^2} \tag{17}$$

With S_{ij}^d the traceless symmetric part of the squared velocity gradient tensor, $\sigma_1 > \sigma_2 > \sigma_3$ the three singular values of $\mathbf{g}$, $G_{ij} = \overline{\Delta_k}^2 g_{ik}g_{jk}$ the gradient model, and $D_j = \overline{\Delta_k}^2 g_{jk}d_k$ the gradient model for the density-velocity correlation subgrid term. Unless otherwise is stated, the functional model constants used are $C^{WALE} = 0.55$, $C^{AMD} = 0.3$, $C^{AMDs} = 0.3$, and $C^{Sigma} = 1.5$.

Tensorial eddy-viscosity models are interesting to take into account the anisotropy of the flow by weighting each component of the subgrid-scale model. One of the bases of modeling is to conserve the generic properties of the filtered Navier-Stokes equations. The theory proposed by Deville *et al.*[42] provides the expression that the stress tensor needs to follow in order to respects the invariance properties:

$$\begin{aligned}\tau_{ij} =& a\left(\mathbf{S_{ij}}\cdot\gamma\otimes\gamma+\gamma\otimes\gamma\cdot\mathbf{S_{ij}}\right)+b\,\gamma\otimes\gamma\cdot\mathbf{S_{ij}}\cdot\gamma\otimes\gamma+c\,\mathbf{S_{ij}}\\ &+(d\,tr(\mathbf{S_{ij}})+e\,\mathbf{S_{ij}}:\gamma\otimes\gamma)\mathbf{I}+e\,tr(\mathbf{S_{ij}}\gamma\otimes\mathbf{e})\end{aligned} \tag{18}$$

Where γ is the unit vector used to represent the axes of a Cartesian coordinate system, $\mathbf{I}$ is the identity matrix, and a, b, c, d and e are coefficients.

In this paper, we test the tensorial model obtained by taking $\gamma = \mathbf{e_x}$, the streamwise direction of the flow, $a = 0.5$, $b = -1$,

and $c = d = e = 0$. Considering the studied configuration of a bi-periodic plane channel flow, this tensorial model is equivalent to the $H^{(4)}$ version of the AMD model proposed by Dupuy *et al.*[4,5]:

$$\tau_{ij}^{H^{(4)}AMD}\left(\mathbf{U},\overline{\Delta}\right) = H_{ij}^{(4)}\tau_{ij}^{AMD}\left(\mathbf{U},\overline{\Delta}\right) \tag{19}$$

With

$$H_{ij}^{(4)} = \begin{pmatrix} 0 & 1 & 1 \\ 1 & 0 & 0 \\ 1 & 0 & 0 \end{pmatrix} \tag{20}$$

In the following, the simulation noted "AMDt+AMDs" involves the tensorial AMD model for the computation of momentum convection subgrid term and the scalar AMD model for the density-velocity correlation subgrid term.

B. Structural models

Structural modeling aims at approximating the subgrid tensor, τ, by constructing it from an evaluation of the filtered velocity or a formal series expansion. They are established with no prior knowledge of the nature of the interaction between the subgrid scales and the resolved scales. Drawbacks of structural models are generally a poor prediction of the dissipation and their inclination to be unstable. Two structural models are investigated.

- Scale similarity model[31]

$$\tau_{ij}^{sim} = C^{sim}\left(\widehat{\widehat{U}_j}\widehat{\widehat{U}_i} - \widehat{\widehat{U}}_j\widehat{\widehat{U}}_i\right) \tag{21}$$

$$\pi_{j}^{sim} = C^{sim}\left(\widehat{\widehat{U}_j}\widehat{\widehat{\phi}} - \widehat{\widehat{U}}_j\widehat{\widehat{\phi}}\right) \tag{22}$$

The scale similarity hypothesis consists in assuming that the statistical structure of the tensor of the subgrid scales is similar to that of the smallest resolved scales. Sagaut[43] explains that this model generally produces good results. However, it is slightly dissipative and tends to underestimate the energy cascade. Box and Laplacian filters are tested for the scale similarity model, associated simulations are respectively noted as "Sim" and "SiL" in Section V. The box filter is computed as an average over three cells in the three directions. The Laplacian filter involves the Taylor series expansion of the box filter using the local cell size as the filter width.

- Gradient model[44]

$$\tau_{ij}^{grd} = \frac{1}{12}C^{grd}\overline{\Delta_k}^2 g_{ik}g_{jk} \tag{23}$$

$$\pi_{j}^{grd} = \frac{1}{12}C^{grd}\overline{\Delta_k}^2 g_{ik}d_k \tag{24}$$

Unless otherwise is stated, the structural model constants used are $C^{Sim} = 1.0$ and $C^{grd} = 1.0$.

C. Mixed models

Mixed modeling aims at combining the advantages of functional and structural models. On the one hand, the functional approaches generally correctly take into account the level of the energy transfers between the resolved and the subgrid scales. On the other hand, the structural models generally produce a good approximation of the structure of the subgrid tensor and are able to capture anisotropic effects and disequilibrium[13,45,46]. We study two mixed models: the multiplicative mixed model (MMG model) proposed by Dupuy *et al.*[6] and a model coupling the tensorial version of the AMD model and the scale similarity model. The multiplicative mixed model based on the gradient model (MMG model) is a functional model constructed such that its magnitude is determined by the gradient model and its orientation is aligned with the rate of deformation tensor or the scalar gradient depending on the subgrid term.

$$\nu_t^{MMG}(\mathbf{g},\mathbf{d}) = -C^{MMG}\frac{G_{kk}}{|\mathbf{S}|} \tag{25}$$

where $C^{MMG} = 0.05$. The second mixed model is the scale similarity associated with the tensorial version of the AMD model for the momentum convection and associated with the scalar AMD for the density-velocity correlation, (sim + AMDt - sim + AMDs).

IV. STUDY CONFIGURATION

A. Channel flow configuration

The study configuration is close to the working conditions of the gas-pressurized solar receivers of concentrated solar power towers. The solar receiver is assumed to be an infinitely long and wide channel. One wall of the channel absorbs concentrated solar light whereas the other is insulated. To reproduce these conditions, thermal large-eddy simulations are performed in a fully developed three-dimensional turbulent channel flow asymmetrically heated. The channel is displayed in Fig. 1. It is periodic in the streamwise (x), and spanwise (z) directions and enclosed by two plane walls in the wall-normal direction (y). The domain size is $4\pi\delta \times 2\delta \times 4/3\pi\delta$ with $\delta = 3$mm. The temperatures of the plates are fixed to 1300 K for the hot wall ($y = 2\delta$) and 900 K for the other wall, designed as cold wall ($y = 0$). The wall temperature ratio is then 1.44. Note that, in gas-pressurized solar receivers the inertia of the walls is important meaning that air is passing through a channel at almost temporally constant wall temperatures. However, neither the temperature nor the heat flux are spatially constant over the walls of the solar receiver. Avellaneda *et al.*[47] show that there are not significant differences between the two types of thermal boundaries conditions for turbulent low Mach channel flow under asymmetric high temperature gradient. The thermodynamical pressure, P_0, is 10 bars. The hot and cold friction Reynolds numbers are respectively 630 and 970, leading to a mean friction Reynolds number of 800.

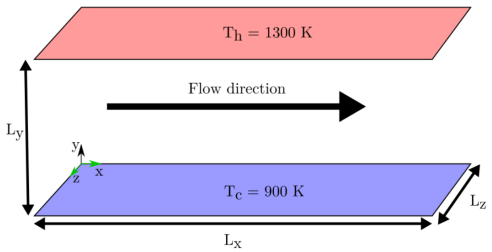

FIG. 1. Geometry of the channel flow. The periodic directions are in green.

B. Numerical settings

Simulations are carried out using a finite difference method in a staggered grid system. Mesh is uniform in the homogeneous directions (x and z) and follows a hyperbolic tangent law in the wall-normal coordinate direction (y). Time derivatives are calculated with a third-order Runge-Kutta scheme. Momentum convection is approached using a fourth-order centered scheme. Velocity divergence, which is the temperature convection, and temperature diffusion are discretized with centered second-order schemes. For mass convection, a Quick and a centered second-order schemes are compared. This last scheme has been used by Streher *et al.*[48] in a LES study dealing with isothermal channel flow and produces very good results. High-resolution spatial discretization methods such as the compact finite difference schemes proposed by Lele[49] are not tested in this study. Indeed, despite their accuracy, they are difficult to implement in complex geometries. Their use would complicate the simulations of more complex geometries of solar receivers. TrioCFD software[50] is used to perform the simulations. This code has been developed by the French Alternative Energies and Atomic Energy Commission and has been used in many simulations of fluid flows[4,5,47,51–53].

$$y_k = L_y\left(1+\frac{1}{a}\tanh\left[\left(\frac{k-1}{N_y-1}\right)\tanh^{-1}(a)\right]\right) \qquad (26)$$

where a is the mesh dilatation parameter and N_y is the number of grid points in the wall-normal direction. The meshes used for DNS and T-LES are given in Table I. For the LES meshes, the first, second, and third characters respectively correspond with the x, y, and z directions. Character "A" stands for the highest resolution tested in a particular direction whereas "E" accounts for the coarsest resolution. The resolution in the wall-normal direction is not studied since it is substantially less impacting the results than the resolution in other directions, as explained by Rezaeiravesh and Liefvendahl[34].

TABLE I. DNS and T-LES mesh characteristics. The dimensionless mesh size is given for the cold wall, which corresponds to the highest friction Reynolds number.

Name	Number of grid points $N_x \times N_y \times N_z$	Dimensionless mesh size Δ_x^+ ; $\Delta_y^+(0)$; $\Delta_y^+(\delta)$; Δ_z^+
DNS	$1152 \times 746 \times 768$	10.7 ; 0.41 ; 5.3 ; 4.1
AAA	$192 \times 152 \times 128$	64 ; 1.0 ; 32 ; 32
BAB	$160 \times 152 \times 96$	77 ; 1.0 ; 32 ; 43
CAC	$128 \times 152 \times 72$	96 ; 1.0 ; 32 ; 57
DAD	$96 \times 152 \times 48$	128 ; 1.0 ; 32 ; 85

V. RESULTS AND DISCUSSION

The results of the simulations are spatially-averaged in the homogeneous directions and are time-averaged. This combination of averages is denoted by $\langle\cdot\rangle$. The T-LES results are assessed with a DNS performed in the same conditions. We investigate mean quantities and covariances. In this work, T-LES models that are traceless, functional models, and partially traceless, mixed models, are studied. For these models, only the deviatoric Reynolds stresses can be reconstructed and compared with DNS data without filtering process[54]. It is the reason why, for the diagonal Reynolds stresses, we compare the DNS deviatoric Reynolds stress tensor, $R_{ij}^{DNS,dev}$, to the LES deviatoric Reynolds stress tensor, $R_{ij}^{LES,dev}$, plus the averaged deviatoric subgrid-scale stress tensor, $\langle\tau_{ij}^{SGS}\rangle^{dev}$:

$$R_{ij}^{DNS,dev} = R_{ij}^{LES,dev} + \langle\tau_{ij}^{SGS}(\mathbf{U},\overline{\Delta})\rangle^{dev}, for\ i=j \qquad (27)$$

where $R_{ij}^{DNS} = \langle U_iU_j\rangle - \langle U_i\rangle\langle U_j\rangle$ and $R_{ij}^{LES} = \langle\widetilde{U_iU_j}\rangle - \langle\widetilde{U_i}\rangle\langle\widetilde{U_j}\rangle$. Note that the coordinates x_1, x_2, x_3 and x, y, z as well as U_1, U_2, U_3 and U, V, W are used interchangeably for practical reasons. As for the off-diagonal Reynolds stresses, the full Reynolds stress tensor is investigated since there is no reconstruction issue.

$$R_{ij}^{DNS} = R_{ij}^{LES} + \langle\tau_{ij}^{SGS}(\mathbf{U},\overline{\Delta})\rangle, \qquad (28)$$

Concerning the velocity-temperature correlations, the same procedure is applied.

$$R_{i\theta}^{DNS} = R_{i\theta}^{LES} + \langle\pi_i^{SGS}(\mathbf{U},T,\overline{\Delta})\rangle \qquad (29)$$

With $R_{i\theta}^{DNS} = \langle U_i\theta\rangle - \langle U_i\rangle\langle\theta\rangle$ and $R_{ij}^{LES} = \langle\widetilde{U_i\theta}\rangle - \langle\widetilde{U_i}\rangle\langle\widetilde{\theta}\rangle$. Here $\pi_i^{SGS}(\mathbf{U},T,\overline{\Delta})$ is linked to $\pi_i^{SGS}(\mathbf{U},1/\overline{\rho},\overline{\Delta})$ by the ratio r/P_0 thanks to ideal gas law.

A "+" superscript following a variable indicates that this variable is normalized with the classical scaling: $x_i^+ = x_iU_\tau/\nu$, $U_i^+ = U_i/U_\tau$, $\langle R_{ij}\rangle^+ = \langle R_{ij}\rangle/U_\tau^2$, and $\langle U_i'\theta'\rangle^+ = \langle U_i'\theta'\rangle/(U_\tau\theta_\tau)$. The friction velocity and the friction temperature are respectively defined as $U_\tau = \sqrt{\nu\partial U/\partial x_2}$, and $\theta_\tau = \phi_w/(\rho C_pU_\tau)$, where ϕ_w is the conductive heat flux at the wall.

In subsection V C, results of 22 T-LES involving the models presented in III are summarized and discussed. Six selected T-LES are detailed in subsection V D.

A. Data processing

This section presents results of T-LES models in order to evaluate their efficiency. T-LES results are compared to DNS using the following procedure. Firstly, we interpolate the DNS wall-normal profiles on the mesh used for T-LES, then values are compared as expressed below :

$$\varepsilon_X^{LES_j} = \frac{\sum_{i=1}^{N_y/2} log\left(\frac{y_{i+1}}{y_i}\right)\left|\left(X_i^{LES_j} - X_i^{DNS}\right)X_i^{LES_j}\right|}{\sum_{i=1}^{N_y} log\left(\frac{y_{i+1}}{y_i}\right)X_i^{DNS^2}} + \frac{\sum_{i=1}^{N_y/2} log\left(\frac{2\delta-y_{i+1}}{2\delta-y_i}\right)\left|\left(X_{Ny/2-i+1}^{LES_j} - X_{Ny/2-i+1}^{DNS}\right)X_{Ny/2-i+1}^{LES_j}\right|}{\sum_{i=1}^{N_y} log\left(\frac{2\delta-y_{i+1}}{2\delta-y_i}\right)X_i^{DNS^2}} \tag{30}$$

Where ε is the error, X is the observed value, LES_j refers to the jth tested model, y_i is the ith node in the wall-normal direction, and δ is the half height of the channel. Note that the logarithmic ratio aims to give more importance to near wall values than to mid-channel values. Moreover, the error calculated in the square root is weighted by the local value to accentuate the importance of peak values.

T-LES models are assessed on 11 physical quantities divided into two groups:

- Mean
  - U, the longitudinal velocity profile,
  - V, the wall-normal velocity profile,
  - T, the temperature profile,
  - ϕ, the normal conductive heat flux at the wall.
- Correlations
  - $\langle u'u'\rangle^{dev}$, the covariance of the longitudinal velocity,
  - $\langle v'v'\rangle^{dev}$, the covariance of the wall-normal velocity,
  - $\langle w'w'\rangle^{dev}$, the covariance of the transversal velocity,
  - $\langle \theta'\theta'\rangle$, the covariance of temperature,
  - $\langle u'v'\rangle$, the correlation of longitudinal and wall-normal velocities,
  - $\langle u'\theta'\rangle$, the correlation of longitudinal velocity and temperature,
  - $\langle v'\theta'\rangle$, the correlation of wall-normal velocity and temperature.

Then, we compute the final error of the jth T-LES model on mean quantities, Err_{mean}, and the final error of the jth T-LES model on covariance, Err_{rms} by adding the error obtained for each value and dividing this sum by the results of the worst model:

$$Err_{mean}^{LES,j} = \frac{\sum_X \varepsilon_X^{LES_j}}{max\left(\sum_X \varepsilon_X^{LES}\right)} \tag{31}$$

where X is successively U, V, T and ϕ.

$$Err_{rms}^{LES,j} = \frac{\sum_X \varepsilon_X^{LES_j}}{max\left(\sum_X \varepsilon_X^{LES}\right)} \tag{32}$$

where X is successively the square root of $\langle u'u'\rangle^{dev}$, $\langle v'v'\rangle^{dev}$, $\langle w'w'\rangle^{dev}$, $\langle \theta'\theta'\rangle$, $\langle u'v'\rangle$, $\langle u'\theta'\rangle$, and $\langle v'\theta'\rangle$.

B. Preparatory study

1. Mesh sensitivity analysis

A mesh sensitivity analysis is carried out in the studied conditions. The four LES meshes exposed in Tab. I are tested. The averaged errors on mean quantities and rms values are presented. The results of each LES mesh are compared with the results obtained with the DNS mesh presented in Tab. I. Fig. 2 displays the errors committed by LES performed (1) without model ("no-model") involving the second-order centered scheme to discretize the mass convection term; (2) with the tensorial model ("AMDt + AMDs") associated with the Quick scheme. The results are sensitive to mesh refinement as classically observed (see for instance Kremer and Bogey[36] and Dupuy *et al.*[4]). The top-graph shows that the error on mean quantities is non-monotonic for the no-model simulations. The best results are obtained with the "BAB" and "CAC" meshes for which the induced numerical dissipation is improving the results. Regarding rms values, the error is decreasing with the mesh refinement. The error committed with "CAC" and "DAD" meshes are truncated on the graph. For the "CAC" mesh, the averaged error on mean quantities is 67%; for the "DAD" mesh, it is 131%. Regarding the "AMDt + AMDs" model (bottom-graph), the errors are decreasing with a monotonic tendency. These results indicate that introducing a model permits to decrease the mesh sensitivity of the error, which is profitable. The improvement of the results on rms values almost reach a plateau for the meshes "AAA" and "BAB". For this reason and its accuracy on mean quantities with the no-model (c2) simulation, the "BAB" mesh is selected in the following. It seems to be a good compromise between the result accuracy and the computational time. The no-model simulations performed with the "BAB" mesh are called ILES thereafter.

2. Evaluation of Implicit Large-Eddy Simulation

In implicit Large-Eddy Simulations (ILES) the truncation error of the discretization scheme is employed to model the

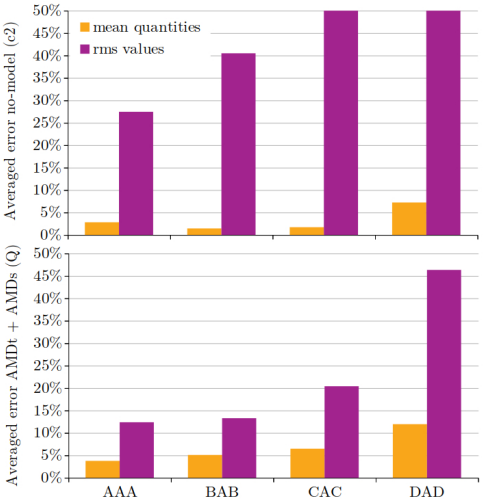

FIG. 2. Averaged errors obtained with four different meshes on mean quantities and rms values. Simulations without model and with the tensorial functional model are studied.

effects of unresolved scales instead of an explicit computation of the SGS stress tensor, see Refs.[14,28,55] for more detail on ILES. Two ILES are tested and compared with the results of the simulations involving turbulence models in the following. The ILES solution combining the selected mesh and numerical scheme (mass convection and momentum convection are respectively approached with a Quick scheme and a fourth-order centered scheme) is compared to a no-model simulation. This no-model simulation aims to reproduce the one performed by Streher *et al.*[48] in an isothermal turbulent channel flow at a friction Reynolds number of 950, see Fig. 3. Note that, this simulation is performed with the same numerical setup as the one of Streher *et al.*, except the time derivatives which are computed with a third order Runge-Kutta scheme instead of a second-order Adams–Bashforth time integration scheme. Moreover, the dimensionless cell sizes are close but not identical. However, the streamwise velocity profile obtained by the no-model simulation is similar to the one obtained by Streher *et al.*[48]. For that reason, this no-model simulation is named "no-model Streher *et al.*" in Fig. 3. The ILES are assessed with the DNS performed by Hoyas and Jiménez[56]. The resolution of the DNS of Hoyas and Jiménez is $\Delta x^+ = 11$, $\Delta y(0)^+ = 0.28$, $\Delta y(\delta)^+ = 7.6$, and $\Delta z^+ = 5.7$. The results show that the proposed ILES, performed with the BAB mesh, gives a very accurate estimation of the streamwise velocity profile and is better than the "no-model Streher *et al.*" simulation. The mesh used by Streher *et al.* is, yet, 1.5 times finer in the streamwise direction and 2 times finer in the spanwise direction than the mesh selected for the ILES. The wall normal resolution of the mesh proposed by Streher *et al.* is $\Delta y^+(0) = 1.5$ and $\Delta y^+(\delta) = 28$. It demonstrates that the numerical dissipation induced by the selected mesh is profitable. It explains the accuracy of the ILES on the prediction of mean quantities observed in the following.

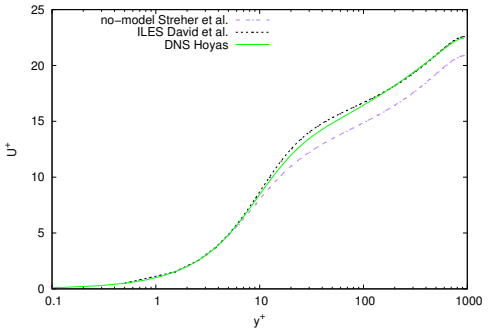

FIG. 3. Comparison of the streamwise velocity profile obtained with the no-model simulation of Streher *et al.* and the proposed ILES (noted as ILES David *et al.*).

C. General results and assessment of LES models

The LES models are tested on the mean quantities and the correlations presented above. Implicit LES are also assessed. As it is difficult to differentiate the numerical error from the model error with *a posteriori* tests, this study aims to propose solutions combining a mesh, a turbulence model, and a numerical scheme. Fig. 4 presents the normalized difference between DNS and various T-LES approaches. The top-graph stands for the T-LES error on mean quantities. The results indicate that the second-order centered scheme significantly improves the efficiency of functional models when regarding the error on mean quantities. The results of the scale similarity model are slightly deteriorated. Concerning mixed models, they are more efficient with the second-order centered scheme. The best results are obtained with the WALE model combined with the second-order centered scheme. Note that, with the used numerical setting, the performance of the implicit LES is satisfying when regarding mean quantities. The middle graph accounts for the T-LES error on correlations. The second-order centered scheme tends to deteriorate the LES correlation prediction of all the models. The best estimation of these values is obtained with the combination of tensorial AMD for the momentum convection subgrid term and scalar AMD for the density-velocity subgrid term. The ILES poorly estimate the correlations. The bottom-graph is the weighted average of the two first histograms and proposes a global error for each T-LES approach. The weight associated with mean quantities is four since there are four mean quantities and the weight related to correlations is seven. Globally, the best results are obtained with the "AMDt + AMDs", followed by the "AMD (c2)" model. Note that the simulation

combining the tensorial AMD and scalar AMD models does not converge when performed with the second-order centered scheme.

We select the "AMD (c2)", "AMDt + AMDs (Q)", "Sim (c2)", and "Sim-AMDt + Sim-AMDs (c2)" models as well as the "ILES (Q)" and the "ILES (c2)" simulations for a more careful analysis.

Fig. 4 highlights the significant effects of the numerical scheme used for the discretization of the mass convection term on the results. Table II shows the results obtained with ILES for both schemes on each value. The mass convection has only low influence on the longitudinal velocity and on the covariances of velocities. However, the choice of the numerical scheme has substantial consequences on the wall-normal velocity. The second-order centered scheme, few dissipative, provides a much better estimation of the wall-normal velocity than the Quick scheme. These good results on the wall-normal velocity affect directly the thermal values by modifying the behavior of turbulent structures. Effects are salient on the conductive heat fluxes at walls, the velocity-temperature correlations, and the fluctuations of temperature. Considering the numerical setup and the working conditions of this study, the second-order centered scheme is much better than the Quick scheme for the heat fluxes and the velocity-temperature correlations. Nonetheless, the Quick scheme is preferable for the prediction of temperature fluctuations.

D. Detailed results of selected models

Results obtained with the selected simulations are detailed here. They are divided into two parts. Firstly, mean quantities are presented then covariances and rms values are studied.

1. Mean quantities

Fig. 5 gives the relative error of the six selected models on the mean quantities. The longitudinal velocity profile is predicted within 4% of error excepted for the AMD model associated with the second-order centered scheme. However, the estimation of the "AMD (c2)" approach on wall-normal velocity is the best. The mixed model is not able to produce a satisfying prediction of the wall-normal velocity profile. It seems that the particular behavior of the scale-similarity model on the hot side is responsible for the poor results of the mixed model on this side. All the models provide a very good estimation of the temperature profile. Lastly, the DNS heat flux is correctly predicted ($\varepsilon < 6\%$) for all models excepted "AMDt + AMDs (Q)". The error committed on the flux is likely due to the Quick scheme used to compute the mass convection. Indeed, similar errors on heat flux are observed for all models when associated with the second-order centered scheme.

The profiles of dimensionless longitudinal velocity, wall-normal velocity, and temperature are plotted as functions of the wall-normal direction (Fig. 6). The top-left graph shows that, excepted the "AMD (c2)" T-LES which tends to overestimate the velocity, the models give a good approximation along with the entire profile of longitudinal velocity. Deviations between T-LES and DNS appear after $y^+ = 15$ and remain almost constant across the logarithmic law. The top-right graph describes the wall-normal velocity profile. This value skyrockets in the buffer layer (from $y^+ = 2$ to $y^+ = 30$) and reaches a constant velocity zone in the logarithmic layer. The "AMDt + AMDs (Q)" approach tends to underestimate the magnitude of the DNS profile. As seen in Fig. 5, the "AMD (c2)" T-LES is better than the other models. Note that, the "ILES (c2)" provides very satisfying results on this profile. Lastly, the temperature profile is analyzed on the bottom-left graph. As for the longitudinal velocity profile, the differences between T-LES and DNS emerge at $y^+ = 15$. However, on the cold side, the scale-similarity and the mixed models are close to the DNS profile. On the hot side, the AMD model and the tensorial AMD model are the best.

2. Covariances and rms values

Covariance and rms values can be seen as second-order statistics since they deal with turbulence structures. They are more complex to predict but gives useful information on the flow. The errors committed on covariances and rms values are exposed in Fig. 7. As expected, the accuracy of the models on covariances and rms values is poorer than the results on mean quantities. The same model ranking is observed for the three velocity fluctuations. The biggest errors are committed on the covariance of transversal velocity. The "AMDt + AMDs (Q)" approach is the best among those studied. The results on the correlation $\langle u'v' \rangle$ are very satisfying for all the models. Once again, the "AMDt + AMDs (Q)" approach produces the best results. It is probably thanks to its tensorial formulation which allows it to reproduce the strong wall-normal anisotropy of channel flow. The temperature fluctuations are more correctly estimated with the mixed model. The correlation between longitudinal velocity and temperature is a substantial challenge for T-LES. With 20% of error, the "AMDt + AMDs (Q)" T-LES produces the closest results to DNS. The correlation of wall-normal velocity and temperature is globally well predicted with an error inferior to 10%. The results of the scale-similarity and the mixed model on the fluctuations of heat flux show a very good agreement with DNS. Those of the "AMDt + AMDs (Q)" approach have 20% of error. The "ILES (c2)" gives a poor approximation of this quantity. The deviatoric part of the diagonal terms of the Reynolds stress tensor and the cross velocity correlation are plotted along the wall-normal direction in Fig. 8. From top-left to bottom-right, the $\langle u'u' \rangle^{dev}$, $\langle v'v' \rangle^{dev}$, $\langle w'w' \rangle^{dev}$, and $\langle u'v' \rangle$ are observed. Regarding the flow behavior, we notice that the peaks of the correlations are bigger on the cold side than on the hot side, despite a higher friction velocity value contributing to the denominator of the dimensionless numbers. This can be due to the reduced local friction Reynolds number on the hot side, also seen in Boutrouche *et al.*[57], Bellec *et al.*[22], and Yahya *et al.*[24]. The three diagonal components of the Reynolds shear stress tensor show a peak around $y^+ = 15$ indicating that the dynamics of the near-wall turbulence is controlled by turbulence struc-

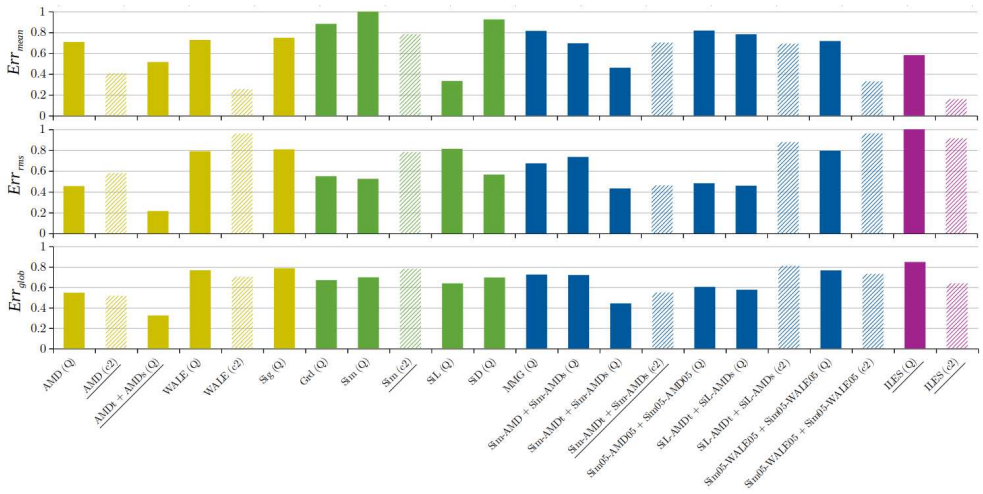

FIG. 4. Normalized error of various T-LES approaches. From top to bottom, the error concerns mean quantities, correlations, and global error. Yellow, green, and blue colors respectively stand for functional, structural, and mixed models. Purple color accounts for ILES. Full bars represent the simulations performed with the Quick scheme for the discretization of the mass convection whereas hatched bars are for T-LES using the second-order centered scheme. The six selected T-LES are underlined.

TABLE II. Comparison of the numerical scheme effect on the error committed by ILES on each variable.

	ε_U	ε_V	ε_T	ε_ϕ	$\varepsilon_{\langle u'u'\rangle^{dev}}$	$\varepsilon_{\langle v'v'\rangle^{dev}}$	$\varepsilon_{\langle w'w'\rangle^{dev}}$	$\varepsilon_{\langle u'v'\rangle}$	$\varepsilon_{\langle u'\theta'\rangle}$	$\varepsilon_{\langle v'\theta'\rangle}$	$\varepsilon_{\langle\theta'\theta'\rangle}$
ILES (Q)	3.2	16.6	0.7	18.7	54.8	40.8	85.4	3.6	19.3	16.7	23.9
ILES (c2)	3.1	1.9	0.5	0.3	51.6	38.5	80.6	4.6	28.4	2.0	77.8

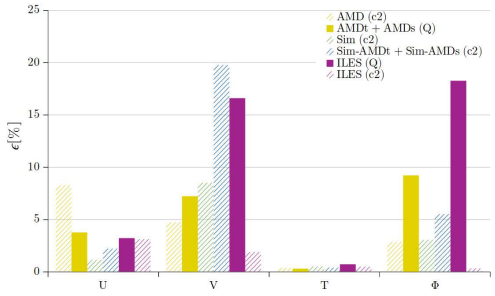

FIG. 5. Relative error on mean quantities for selected T-LES approaches. Yellow, green, and blue colors respectively stand for functional, structural, and mixed models. Full bars represent the simulations performed with the Quick scheme for the discretization of the mass convection whereas hatched bars are for T-LES using the second-order centered scheme.

tures present is this region. On the hot side, the peak is slightly shifted toward the wall. The T-LES models tend to overestimate the $\langle u'u'\rangle^{dev}$, $\langle v'v'\rangle^{dev}$, and $\langle w'w'\rangle^{dev}$ peaks at both sides of the channel. This tendency is also observed by Dupuy *et al.*[4]. The tensorial model produces very good estimation of the velocity covariances on the hot side. The scale similarity model gives the worst approximation, probably because its poorly dissipative behavior induces an overestimation of turbulence levels. Indeed, the scale-similarity model does not take into account the smallest unresolved scales where the most dissipation of turbulent subgrid-scale energy takes place. This lack of dissipation should be responsible for the exaggerated fluctuations of velocities predicted by the scale-similarity model. The cross-correlation $\langle u'v'\rangle$ is well captured by all T-LES.

Fig. 9 depicts the correlation of longitudinal velocity and temperature, the correlation of wall-normal velocity and temperature, and the covariance of temperature. The $\langle u'\theta'\rangle$ correlation exhibits peaks around $y^+ = 15$. Once again, the cold side presents a bigger peak than the hot side. These high values of $\langle u'\theta'\rangle$ are due to the streaks encountered in the buffer layer. Apart from the tensorial model, all T-LES overestimate the peaks. This overestimation is moderate on the hot side but substantial on the cold side. Concerning the "AMDt + AMDs (Q)" model, it underestimates the peaks. The tensorial formulation must be responsible for these encouraging results of the turbulent streamwise heat flux. The better re-

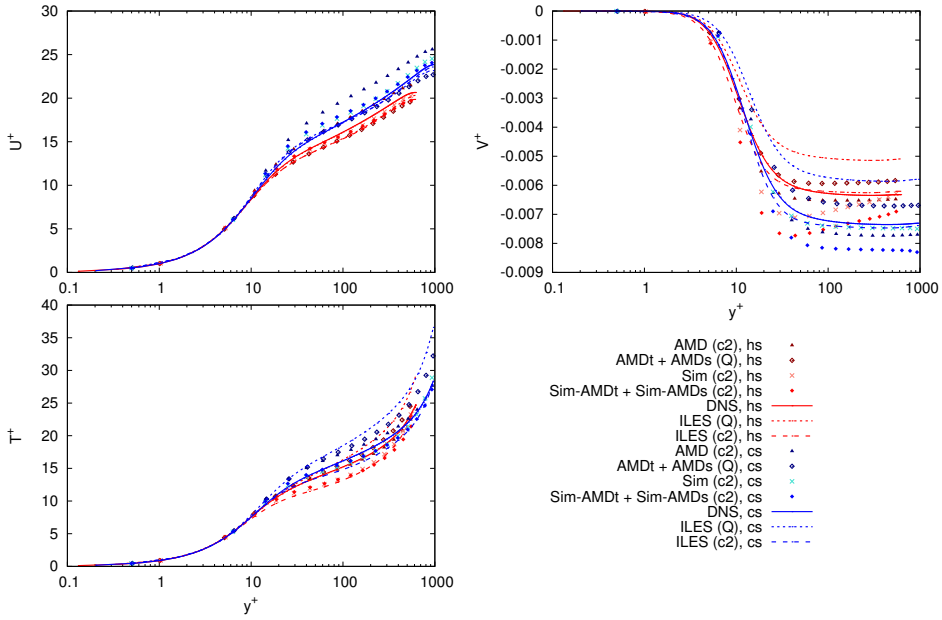

FIG. 6. Profiles of dimensionless longitudinal velocity, wall-normal velocity and temperature along the wall-normal direction of the channel.

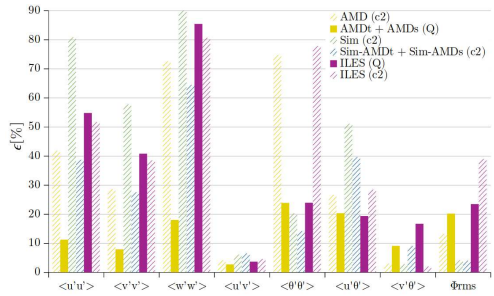

FIG. 7. Relative error on covariances for selected T-LES approaches. Yellow, green, and blue colors respectively stand for functional, structural, and mixed models. Full bars represent the simulations performed with the Quick scheme for the discretization of the mass convection whereas hatched bars are for T-LES using the second-order centered scheme.

sults of the models on the hot side are probably due to a finer dimensionless cell size which improves the prediction of near-wall behaviors. The propagated errors from the viscous sublayer to the buffer layer are then lower on the hot side. The $\langle v'\theta'\rangle$ correlation is displayed. The profile is characterized by a strong increase of the correlation in absolute value in the range $y^+ \in [4;20]$, as observed for the wall-normal velocity profile. T-LES estimations are good. The $\langle v'\theta'\rangle$ DNS profile is particularly well approximated on the hot side. It is probably due to the finer relative mesh size when compared to as the cold side. On the cold side, the "AMD (c2)" and "AMDt + AMDs (Q)" approaches give the best results. We observe that the fluctuations of temperature are constituted of three peaks. The biggest fluctuations are reached in the centerline because of packets of hot and cold fluid that come from the walls and collect near the centerline, as observed by Johansson and Wikström[58]. The two secondary peaks are located at $y^+ = 15$. Regarding the LES models, the best approximation of the dimensionless covariance of temperature is obtained with the "AMDt + AMDs (Q)" model. Indeed, this approach provides a very accurate estimation of the dimensionless covariance temperature profile. The scalar AMD, specifically devised to model the density-velocity correlation and consistent with the exact subfilter stress tensor on anisotropic grids, is probably responsible for these good results.

3. *Instantaneous fields*

Instantaneous fields are helpful to analyze fluid behavior. It is also a good means to assess the effects of LES subgrid-scale

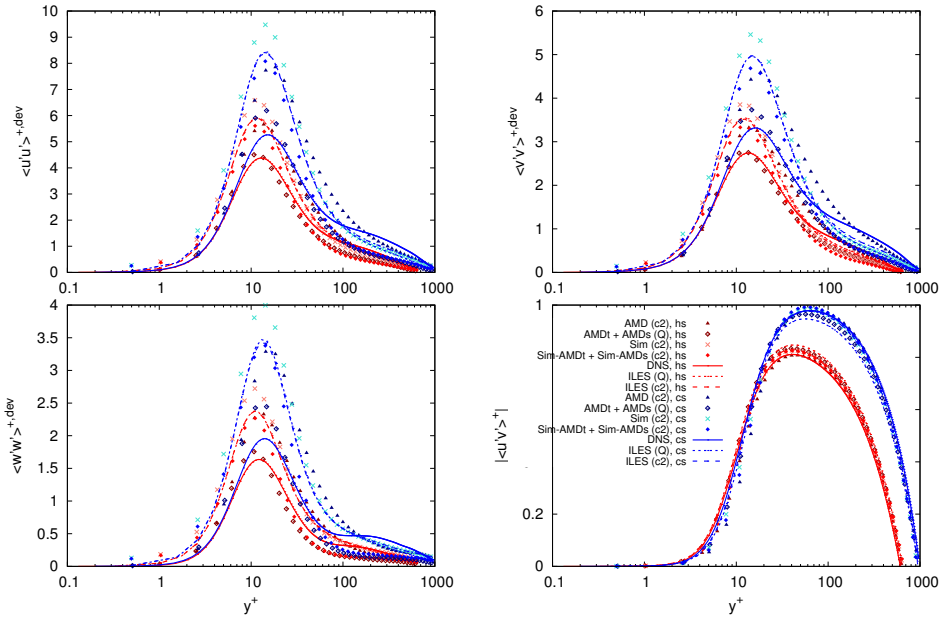

FIG. 8. Profiles of dimensionless covariances of longitudinal velocity, wall-normal velocity, transversal velocity as well as longitudinal and wall-normal velocities along the wall-normal direction of the channel. Note that the absolute value of the $\langle u'v' \rangle^+$ is plotted.

models and numerical schemes.

Firstly, the probability density of normalized heat flux are presented in Fig. 10. The dimensionless conductive wall heat flux is computed using Eq. 33.

$$\phi^* = \frac{\phi - \phi_{mean}}{\phi_{plot,max} - \phi_{mean}} \tag{33}$$

Where $\phi_{plot,max} = 260\ kW/m^2$ is the biggest considered value of heat flux for plots of instantaneous wall heat flux in Fig. 11. For each density probability of each model, six instantaneous fields of wall heat flux have been averaged in order to obtain smooth curves. Since the density probability observed at hot and cold walls are similar, data of both hot and cold side have been used. For all simulations, the maximum probability is reached for a normalized heat flux slightly lower than the mean heat flux. The peak location of the "AMD (c2)" and "ILES (c2)" simulation is similar to that of DNS. For the other simulations, the maximum is reached for values closer to the mean heat flux. The magnitude of T-LES heat flux density probability is bigger than the results of DNS and the peak is thinner than that of DNS. It traduces the underestimation of the heat flux fluctuations. The "AMD (c2)" simulation provides good results in spite of its slight overestimation of the maximum.

The instantaneous fields of hot and cold wall heat fluxes are displayed in Fig. 11. From top to bottom, the simulations "DNS", "ILES (c2)", "ILES (Q)", "AMD (c2)", and "AMDt + AMDs (Q)" are presented. "Sim (c2)" and "Sim-AMDt+Sim-AMDs (c2)" are not displayed because they are respectively similar to "AMDt + AMDs (Q)" and "ILES (Q)". The pseudocolor maps of DNS are covered by small red stains representing high heat fluxes. Those high values are due to high-frequency turbulent structures which increase the wall-normal convection and bring fluid masses at low temperatures close to the wall. The fluid behavior induces better heat transfer in those regions. The DNS maximum wall heat flux ($637\ kW/m^2$) is more than six times bigger than the mean heat flux ($97\ kW/m^2$). Blue zones, traducing very low heat transfer, appear to be linked to long structures oriented toward the streamwise direction. These stains may reveal the presence of streaks above the viscous sublayer of the involved regions. The T-LES patterns of heat fluxes show the same behaviors: small regions of high flux and long zones of low flux oriented toward the streamwise direction. Simulations performed with the Quick scheme tend to underestimate the mean heat flux and the fluctuations. Simulations performed with the second-order centered scheme produce results similar to DNS. However, when the Quick scheme is used, high values of heat flux are truncated. The "AMDt + AMDs" model counterbalance

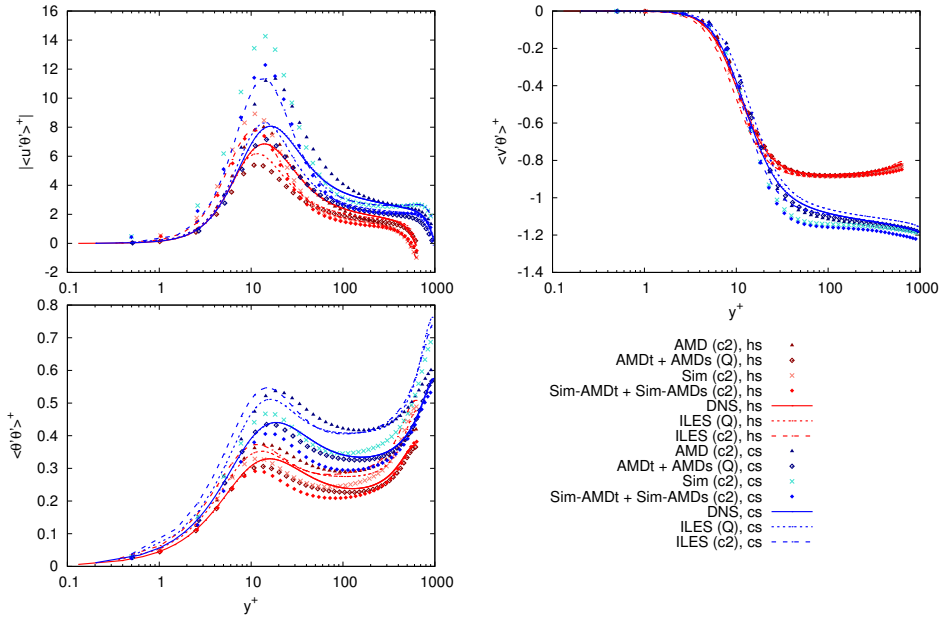

FIG. 9. Profiles of dimensionless correlations of longitudinal velocity and temperature, wall-normal velocity and temperature as well as the covariance of temperature along the wall-normal direction of the channel. Note that the absolute value of the $\langle u'\theta'\rangle^+$ is plotted.

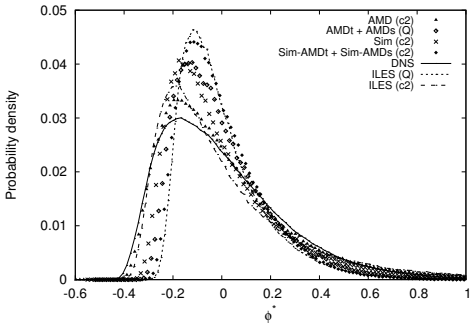

FIG. 10. Probability density of normalized heat flux.

somewhat this behavior but its effect is not enough impactful.

VI. CONCLUSION

In this paper, LES turbulence models and implicit T-LES are compared to DNS results. A Quick and a second-order centered schemes are tested for the discretization of the mass convection term. Firstly, 22 T-LES approaches are assessed on mean quantities and correlations. Six of them are selected for a more accurate analysis. A comparison of these T-LES is performed for each mean quantity and each correlation by integrating the error committed by simulations. We also evaluate the conductive heat flux fluctuations at walls. Moreover, the mean quantities and correlations are plotted as functions of wall-normal distance. Lastly, instantaneous fields of selected T-LES approaches are investigated.

The results indicate that, considering the numerical setup used, the ILES involving the second-order centered scheme contests the best T-LES models studied in this paper on mean quantities. However, the investigation of covariance, rms heat flux, and instantaneous fields highlights the limits of the ILES performed in this study.

As expected, the comparison of the Quick scheme and the second-order centered scheme for the discretization of the mass convection term points out that the streamwise velocity and the Reynolds shear stresses are not significantly influenced by the choice of the numerical scheme. Neverthe-

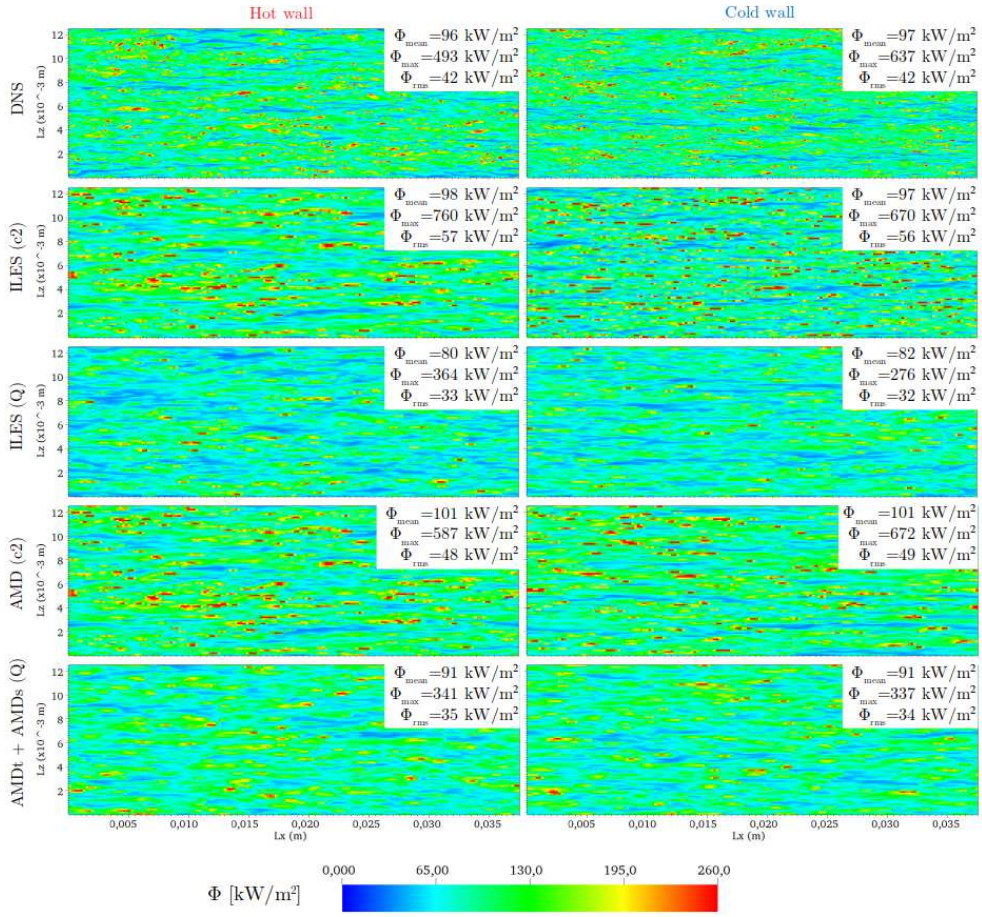

FIG. 11. Instantaneous fields of hot and cold wall heat fluxes. Pictures on the left (respectively right) side correspond to the hot (respectively cold) wall.

less, the numerical scheme effect is substantial on the wall-normal velocity, the conductive wall heat-flux, and the correlations involving the temperature. The T-LES performed with the Quick scheme tends to underestimate the conductive wall heat flux. The second-order centered scheme permits to significantly improve the results on this quantity. This scheme improves the results on the wall-normal velocity as well as the correlation of wall-normal velocity and temperature but it does not impact the wall-normal velocity variances and covariances with streamwise velocity and deteriorates the temperature correlation. This partial improvement suggests that the second order-centered scheme modifies the turbulent structures obtained with DNS simulation. Considering the mean heat flux and the density probability, the best agreement is found with the AMD model combined to the centered scheme.

The T-LES combining the tensorial AMD model to compute the momentum convection and the scalar AMD for the density-velocity correlation, and involving the Quick scheme provides a satisfying estimation of mean quantities and very good results on the classical "+" scaling of correlations. The superiority of this T-LES approach is particularly salient on the covariances of velocities. This result indicates that the tensorial AMD model is able to take into account the anisotropy of the flow.

The studied mixed models provide encouraging results. However, the results obtained show that those models require further investigation in order to benefit of the advantages of

the functional and structural methods.

ACKNOWLEDGMENTS

The authors gratefully acknowledge the CEA for the development of the TRUST platform. This work was granted access to the HPC resources of CINES under the allocation 2019-A0062A05099 and 2020-A0082A05099 made by GENCI. The authors also acknowledge the Occitania region for their funding of the thesis grant.

DATA AVAILABILITY STATEMENTS

The data that support the findings of this study are available from the corresponding author upon reasonable request.

[1]J. B. Chapelier and G. Lodato, "A spectral-element dynamic model for the Large-Eddy simulation of turbulent flows," Journal of Computational Physics **321**, 279–302 (2016).
[2]M. Terracol, P. Sagaut, and C. Basdevant, "A Time Self-adaptive Multilevel Algorithm for Large-eddy Simulation," J. Comput. Phys. **184**, 339–365 (2003).
[3]Y. M. Lee, H. G. Hwang, J. H. Lee, J. Lee, and J. S. Park, "Assessment of two-parameter mixed models for large eddy simulations of transitional and turbulent flows," Journal of Mechanical Science and Technology **34**, 727–743 (2020).
[4]D. Dupuy, A. Toutant, and F. Bataille, "A posteriori tests of subgrid-scale models in strongly anisothermal turbulent flows," Physics of Fluids **31**, 065113 (2019).
[5]D. Dupuy, A. Toutant, and F. Bataille, "A posteriori tests of subgrid-scale models in an isothermal turbulent channel flow," Physics of Fluids **31**, 045105 (2019).
[6]D. Dupuy, A. Toutant, and F. Bataille, "A priori tests of subgrid-scale models in an anisothermal turbulent channel flow at low mach number," International Journal of Thermal Sciences **145**, 105999 (2019).
[7]S. Serra, A. Toutant, and F. Bataille, "Thermal Large Eddy Simulation in a Very Simplified Geometry of a Solar Receiver," Heat Transfer Engineering **33**, 505–524 (2012).
[8]C. Brun, M. Petrovan Boiarciuc, M. Haberkorn, and P. Comte, "Large eddy simulation of compressible channel flow," Theoretical and Computational Fluid Dynamics **22**, 189–212 (2008).
[9]L. D. Dailey, N. Meng, and R. H. Pletcher, "Large Eddy Simulation of Constant Heat Flux Turbulent Channel Flow With Property Variations: Quasi-Developed Model and Mean Flow Results," Journal of Heat Transfer **125**, 27–38 (2003).
[10]E. Lenormand, P. Sagaut, and L. T. Phuoc, "Large eddy simulation of subsonic and supersonic channel flow at moderate Reynolds number," International Journal for Numerical Methods in Fluids **32**, 369–406 (2000).
[11]S. Singh, D. You, and S. T. Bose, "Large-eddy simulation of turbulent channel flow using explicit filtering and dynamic mixed models," Physics of Fluids **24**, 085105 (2012).
[12]W. Rozema, H. J. Bae, P. Moin, and R. Verstappen, "Minimum-dissipation models for large-eddy simulation," Physics of Fluids **27**, 085107 (2015).
[13]U. Piomelli, G. N. Coleman, and J. Kim, "On the effects of nonequilibrium on the subgrid-scale stresses," Physics of Fluids **9**, 2740–2748 (1997).
[14]S. Hickel and N. A. Adams, "On implicit subgrid-scale modeling in wall-bounded flows," Physics of Fluids **19**, 105106 (2007).
[15]M. H. Silvis, R. A. Remmerswaal, and R. Verstappen, "Physical consistency of subgrid-scale models for large-eddy simulation of incompressible turbulent flows," Physics of Fluids **29**, 015105 (2017).
[16]F. Nicoud, H. B. Toda, O. Cabrit, S. Bose, and J. Lee, "Using singular values to build a subgrid-scale model for large eddy simulations," Physics of Fluids **23**, 085106 (2011).
[17]W. Wang and R. H. Pletcher, "On the large eddy simulation of a turbulent channel flow with significant heat transfer," Physics of Fluids **8**, 3354–3366 (1996).
[18]M. Germano, U. Piomelli, P. Moin, and W. H. Cabot, "A dynamic subgrid-scale eddy viscosity model," Physics of Fluids A: Fluid Dynamics **3**, 1760–1765 (1991).
[19]P. Moin, K. Squires, W. Cabot, and S. Lee, "A dynamic subgrid-scale model for compressible turbulence and scalar transport," Physics of Fluids A: Fluid Dynamics **3**, 2746–2757 (1991).
[20]F. Nicoud, "Conservative High-Order Finite-Difference Schemes for Low-Mach Number Flows," Journal of Computational Physics **158**, 71–97 (2000).
[21]B. Lessani and M. V. Papalexandris, "Numerical study of turbulent channel flow with strong temperature gradients," International Journal of Numerical Methods for Heat & Fluid Flow **18**, 545–556 (2008).
[22]M. Bellec, A. Toutant, and G. Olalde, "Large Eddy Simulations of thermal boundary layer developments in a turbulent channel flow under asymmetrical heating," Computers & Fluids A special issue in honor of Cecil "Chuck" E. Leith, **151**, 159–176 (2017).
[23]F. Nicoud and F. Ducros, "Subgrid-Scale Stress Modelling Based on the Square of the Velocity Gradient Tensor," Flow, Turbulence and Combustion **62**, 183–200 (1999).
[24]S. M. Yahya, S. F. Anwer, and S. Sanghi, "Turbulent forced convective flow in an anisothermal channel," International Journal of Thermal Sciences **88**, 84–95 (2015).
[25]S. Serra, E. Franquet, V. Boutrouche, and R. Manceau, "Asymmetric reverse transition phenomenon in internal turbulent channel flows due to temperature gradients," International Journal of Thermal Sciences **159**, 106463 (2021).
[26]C. Meneveau and J. Katz, "Scale-Invariance and Turbulence Models for Large-Eddy Simulation," Annual Review of Fluid Mechanics **32**, 1–32 (2000).
[27]B. Kosović, D. I. Pullin, and R. Samtaney, "Subgrid-scale modeling for large-eddy simulations of compressible turbulence," Physics of Fluids **14**, 1511–1522 (2002).
[28]S. Hickel, N. A. Adams, and J. A. Domaradzki, "An Adaptive Local Deconvolution Method for Implicit LES," J. Comput. Phys. **213**, 413–436 (2006).
[29]S. Vashishtha, R. Samuel, A. G. Chatterjee, R. Samtaney, and M. K. Verma, "Large eddy simulation of hydrodynamic turbulence using renormalized viscosity," Physics of Fluids **31**, 065102 (2019).
[30]K. Horiuti, "The role of the Bardina model in large eddy simulation of turbulent channel flow," Physics of Fluids A: Fluid Dynamics **1**, 426–428 (1989).
[31]J. Bardina, J. Ferziger, and W. Reynolds, "Improved subgrid-scale models for large-eddy simulation," in *13th Fluid and PlasmaDynamics Conference*, Fluid Dynamics and Co-located Conferences (American Institute of Aeronautics and Astronautics, 1980).
[32]S. Stolz, N. A. Adams, and L. Kleiser, "An approximate deconvolution model for large-eddy simulation with application to incompressible wall-bounded flows," Physics of Fluids **13**, 997–1015 (2001).
[33]B. Vreman, B. Geurts, and H. Kuerten, "Comparison of numerical schemes in large-eddy simulation of the temporal mixing layer," International journal for numerical methods in fluids **22**, 297–312 (1996).
[34]S. Rezaeiravesh and M. Liefvendahl, "Effect of grid resolution on large eddy simulation of wall-bounded turbulence," Physics of Fluids **30** (2018), 10.1063/1.5025131.
[35]B. J. Geurts and F. van der Bos, "Numerically induced high-pass dynamics in large-eddy simulation," Physics of Fluids **17**, 125103 (2005).
[36]F. Kremer and C. Bogey, "Large-eddy simulation of turbulent channel flow using relaxation filtering: Resolution requirement and Reynolds number effects," Computers & Fluids **116**, 17–28 (2015).
[37]A. Keating, U. Piomelli, E. Balaras, and H.-J. Kaltenbach, "A priori and a posteriori tests of inflow conditions for large-eddy simulation," Physics of Fluids **16**, 4696–4712 (2004).
[38]S. Paolucci, "Filtering of sound from the Navier-Stokes equations." NASA STI/Recon Technical Report N **83** (1982).
[39]M. V. Papalexandris, "On the applicability of Stokes' hypothesis to low-Mach-number flows," Continuum Mechanics and Thermodynamics **32**, 1245–1249 (2020).

[40]W. Sutherland, "The viscosity of gases and molecular force," The London, Edinburgh, and Dublin Philosophical Magazine and Journal of Science **36**, 507–531 (1893).
[41]M. Abkar, H. J. Bae, and P. Moin, "Minimum-dissipation scalar transport model for large-eddy simulation of turbulent flows," Physical Review Fluids **1**, 041701 (2016).
[42]M. O. Deville and T. B. Gatski, *Mathematical Modeling for Complex Fluids and Flows* (Springer Berlin Heidelberg, Berlin, Heidelberg, 2012).
[43]P. Sagaut, *Large Eddy Simulation for Incompressible Flows*, 3rd ed. (Springer, 1998).
[44]A. Leonard, "Energy Cascade in Large-Eddy Simulations of Turbulent Fluid Flows," in *Advances in Geophysics*, Turbulent Diffusion in Environmental Pollution, Vol. 18, edited by F. N. Frenkiel and R. E. Munn (Elsevier, 1975) pp. 237–248.
[45]R. Akhavan, A. Ansari, S. Kang, and N. Mangiavacchi, "Subgrid-scale interactions in a numerically simulated planar turbulent jet and implications for modelling," Journal of Fluid Mechanics **408**, 83–120 (2000).
[46]C. Meneveau and J. Katz, "Conditional subgrid force and dissipation in locally isotropic and rapidly strained turbulence," Physics of Fluids **11**, 2317–2329 (1999).
[47]J. M. Avellaneda, F. Bataille, and A. Toutant, "DNS of turbulent low Mach channel flow under asymmetric high temperature gradient: Effect of thermal boundary condition on turbulence statistics," International Journal of Heat and Fluid Flow **77**, 40–47 (2019).
[48]L. B. Streher, M. H. Silvis, P. Cifani, and R. W. C. P. Verstappen, "Mixed modeling for large-eddy simulation: The single-layer and two-layer minimum-dissipation-Bardina models," AIP Advances **11**, 015002 (2021).
[49]S. K. Lele, "Compact finite difference schemes with spectral-like resolution," Journal of Computational Physics **103**, 16–42 (1992).
[50]C. Calvin, O. Cueto, and P. Emonot, "An object-oriented approach to the design of fluid mechanics software," ESAIM: Mathematical Modelling and Numerical Analysis - Modélisation Mathématique et Analyse Numérique **36**, 907–921 (2002).
[51]A. Toutant, "Numerical simulations of unsteady viscous incompressible flows using general pressure equation," Journal of Computational Physics **374**, 822–842 (2018).
[52]F. Aulery, D. Dupuy, A. Toutant, F. Bataille, and Y. Zhou, "Spectral analysis of turbulence in anisothermal channel flows," Computers & Fluids A special issue in honor of Cecil "Chuck" E. Leith, **151**, 115–131 (2017).
[53]M. David, A. Toutant, and F. Bataille, "Numerical development of heat transfer correlation in asymmetrically heated turbulent channel flow," International Journal of Heat and Mass Transfer **164**, 120599 (2021).
[54]G. S. Winckelmans, H. Jeanmart, and D. Carati, "On the comparison of turbulence intensities from large-eddy simulation with those from experiment or direct numerical simulation," Physics of Fluids **14**, 1809–1811 (2002).
[55]J. A. Domaradzki and N. A. Adams, "Direct modelling of subgrid scales of turbulence in large eddy simulations," Journal of Turbulence **3**, N24 (2002).
[56]S. Hoyas and J. Jiménez, "Reynolds number effects on the Reynolds-stress budgets in turbulent channels," Physics of Fluids **20**, 101511 (2008).
[57]V. Boutrouche, E. Franquet, S. Serra, and R. Manceau, "Influence of the turbulence model for channel flows with strong transverse temperature gradients," International Journal of Heat and Fluid Flow **70**, 79–103 (2018).
[58]A. V. Johansson and P. M. Wikström, "DNS and Modelling of Passive Scalar Transport in Turbulent Channel Flow with a Focus on Scalar Dissipation Rate Modelling," Flow, Turbulence and Combustion **63**, 223 (2000).

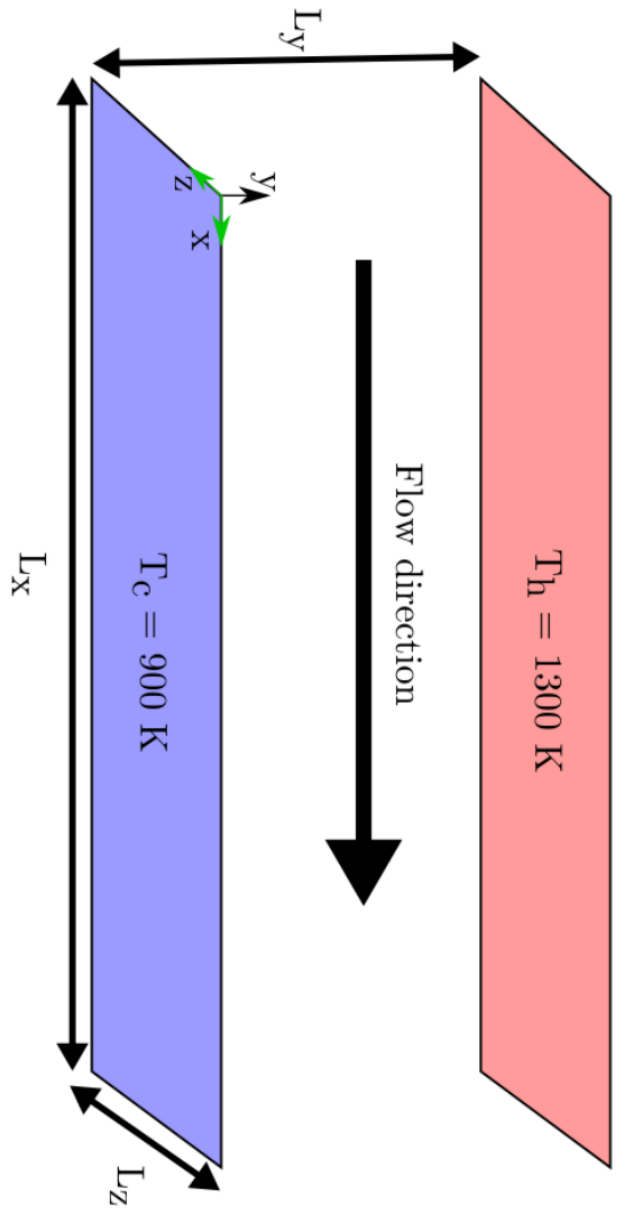

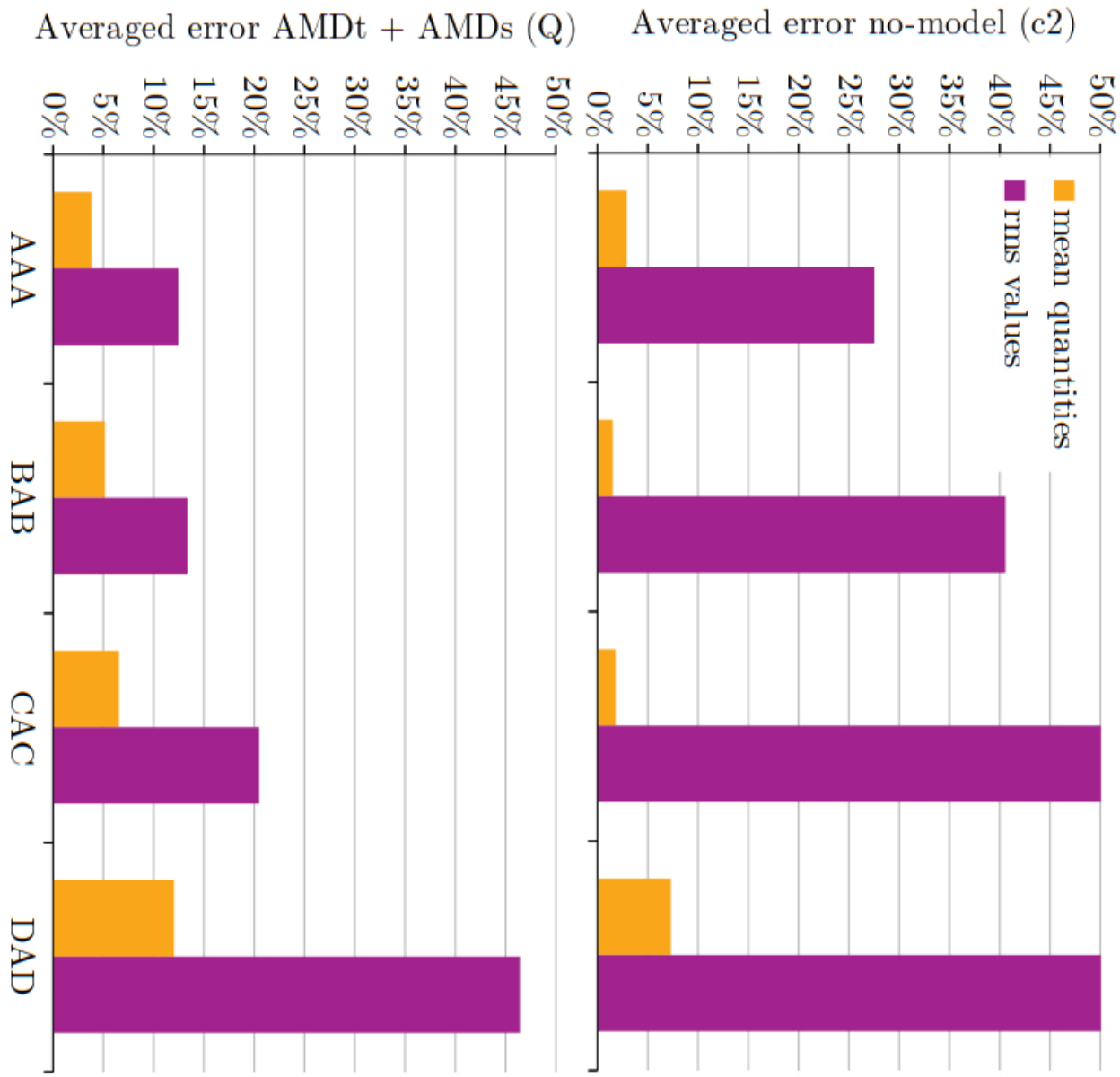

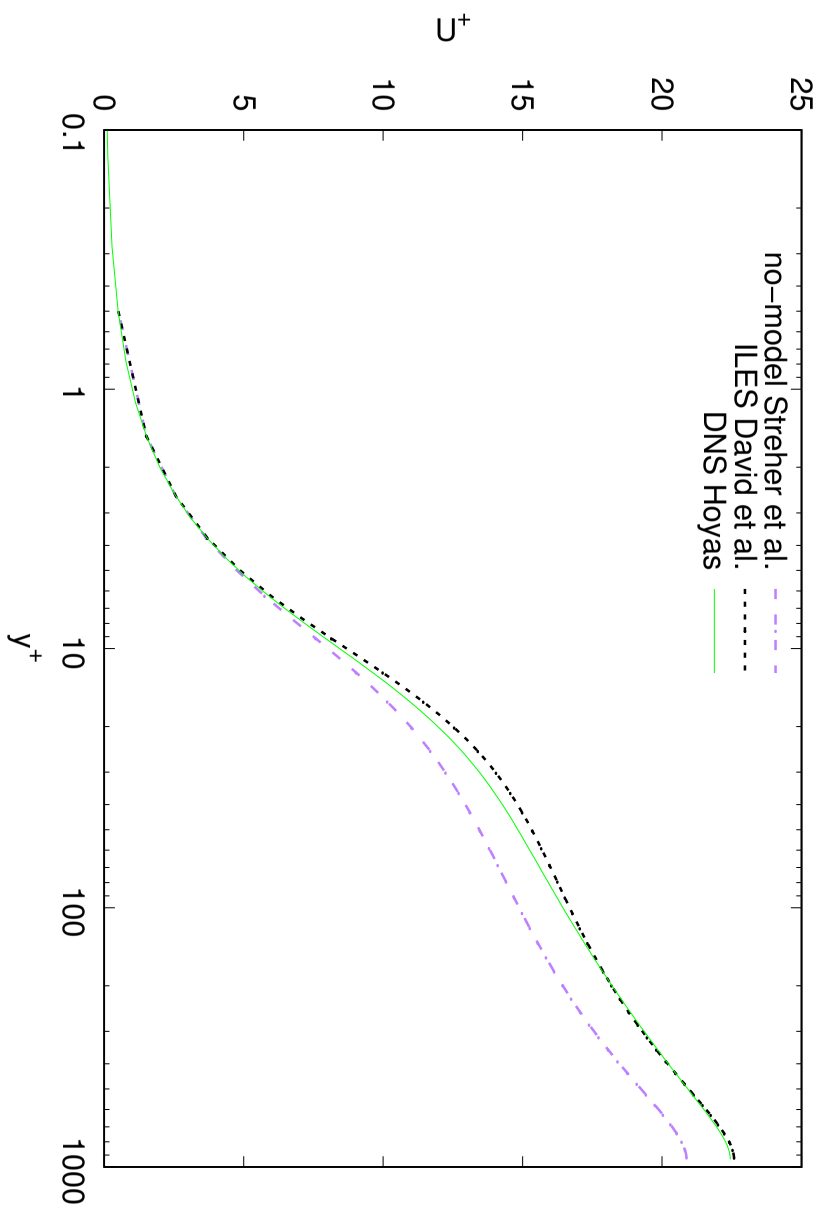

PLEASE CITE THIS ARTICLE AS DOI: 10.1063/5.0040539